Molecular dynamic simulation of thermal transport in monolayer $C_3B_xN_{1-x}$ alloy

Bowen Yang[1]**, Dan Han**[2]**, Xinyu Wang**[2] ⓘ**, Shiqian Hu**[3]**, Qian Xin**[4] ⓘ**,
Bing-Yang Cao**[1,5] **and Gongming Xin**[1] ⓘ

[1] School of Energy and Power Engineering, Shandong University, Jinan 250061, People's Republic of China
[2] Institute of Thermal Science and Technology, Shandong University, Jinan 250061, People's Republic of China
[3] Department of Mechanical Engineering, The University of Tokyo, Tokyo 113-8656, Japan
[4] Center of Nanoelectronics and School of Microelectronics, Shandong University, Jinan 250100, People's Republic of China
[5] Key Laboratory for Thermal Science and Power Engineering of Ministry of Education, Department of Engineering Mechanics, Tsinghua University, Beijing 100084, People's Republic of China

E-mail: xingm@sdu.edu.cn

Abstract

Recently, two-dimensional (2D) monolayers C_3B and C_3N attract growing research interest due to the excellent physical properties. In this work, the thermal conductivities (k) of the monolayer $C_3B_xN_{1-x}$ alloy and the special $C_3B_{0.5}N_{0.5}$ superlattice ($C_3B_{0.5}N_{0.5}$-SL) alloy are systematically evaluated by using molecular dynamic simulation. First, the k of monolayer $C_3B_xN_{1-x}$ alloy presents a U-shaped profile with the increasing random doping ratio (x), in which the lowest k exists in $x = 0.5$. Second, we further calculate the thermal conductivity of $C_3B_{0.5}N_{0.5}$-SL. The result shows an initial decreasing and then rising trend, and the coherent length is 5.11 nm which occupies the minimum thermal conductivity. Furthermore, to uncover the phonon thermal transport mechanism, we calculate the spatiotemporal thermal transport, phonon density of states, phonon group velocity, participation ratio and the phonon wave packet simulations in monolayer alloy system. We note that on account of the random doping atoms, the enhancive phonon-impurity scattering and phonon localization reduce the thermal conductivity in monolayer $C_3B_xN_{1-x}$ alloy. In $C_3B_{0.5}N_{0.5}$-SL, when the period length is smaller than the coherent length, coherent phonon modes emerge because of the phonon interference, in which the superlattice can be regarded as a 'newly generated material'. However, when the period length is larger than the coherent length, the decreasing number of the interface in superlattice lessens phonon-interface scattering and cause the increasing thermal conductivity. This work contributes the fundamental knowledge for thermal management in 2D monolayer $C_3B_xN_{1-x}$ alloy based nanoelectronics.

Keywords: monolayer $C_3B_xN_{1-x}$ alloy, thermal conductivity, molecular dynamic simulation, phonon wave packet simulation

(Some figures may appear in colour only in the online journal)

1. Introduction

Due to the extraordinary properties in thermal [1], electrical [2], mechanical [3] and magnetic [4], two-dimensional (2D) materials have got great attention [5] in both academia and industries. Graphene [6] is one of the most well-known 2D carbon material with honeycomb structure accompanying with the high thermal conductivity (k) [7] and the electrical performance [8]. However, the absence of band gap feature in graphene restricts the direct application in nanoelectronics [9], such as field effect transistors (FETs), solar cells, light emitting diode. Therefore, it is imperative to explore new 2D materials which possess the adjustable

band gap. 2D carbon-boride (C$_3$B) [10] and carbon-nitride (C$_3$N) [11] are also monolayers with honeycomb lattices, which could be considered as important chemical derivative of graphene doped by boron (B) and nitrogen (N) atoms, respectively. Monolayers C$_3$B and C$_3$N possess the indirect band gap about 0.5 eV [12] and 0.39 eV [11], which can be used in FETs [13, 14] and single electron transistors [15]. The monolayer C$_3$N based back-gated FETs show an electrical performance of average on/off current ratio, average electrical mobility and hole mobility as 5.5×10^{10}, $1.2\,\mathrm{cm}^2\,\mathrm{V}^{-1}\,\mathrm{s}^{-1}$ and $1.5\,\mathrm{cm}^2\,\mathrm{V}^{-1}\,\mathrm{s}^{-1}$ [11], respectively. Moreover, the addition of B and N atoms into graphene is an efficient method to tune the electrical properties [16, 17]. Wu *et al* [16] using chemical vapor deposition method doped B and N atoms into monolayer graphene to modify the electrical performances of graphene intrinsically. The doping ratios of B and N atoms were modulated from 0.7% to 4.3% and from 0.9% to 4.8%, the corresponding mobilities of the B and N doped graphene-based back-gate FETs were 450–650 cm^{2}V^{-1} s^{-1} and 350–550 cm^{2}V^{-1} s^{-1}, respectively. Furthermore, by co-doping the B and N atoms in graphene, the electron mobility and hole mobility in doped graphene can attain $8.8 \times 10^3\,\mathrm{cm}^2\,\mathrm{V}^{-1}\,\mathrm{s}^{-1}$ and $12.9 \times 10^3\,\mathrm{cm}^2\,\mathrm{V}^{-1}\,\mathrm{s}^{-1}$, respectively [17].

In practical applications, the heat accumulation can degrade the nanoelectronic device performance and cause unexpected structural failures. To obtain a good electrical performance and long lifetime, the thermal properties play a crucial role in thermal management within the nanoelectronic device [18]. It has been reported that the thermal conductivity values of monolayer graphene generally were within the scope of ~2000–4000 W m^{-1} K^{-1} at room temperature [19]. The modification of the sp2 lattice in pure graphene by substituting C atoms with B and N atoms made the lower thermal conductivities in monolayers C$_3$B and C$_3$N, which were 489 W m^{-1} K^{-1} [20] and 820 W m^{-1} K^{-1} [21]. The B and N atoms act as the phonon-impurity scattering core, which can minish the phonon thermal transport capacity in monolayers C$_3$B and C$_3$N in comparison with the pure graphene. Similarly, the synthesis of random B and N atoms in monolayer graphene is considered to be an efficient approach to regulate the thermal conductivity. Mortazavi *et al* [22] doped 0.75% concentration of B atoms into monolayer graphene, the thermal conductivity reduced more than 60% and vanished the chirality effect. The *k* of N doped graphene was investigated as a function of the doping ratio by using molecular dynamics (MD) simulation. When the doping ratio increased from 0.5% to 7%, the reduction ratios of thermal conductivity in doped graphene were from 62% to 19% [23]. Furthermore, Wang *et al* [24] evaluated the thermal conductivity in doped graphene by embedding the boron nitride (h-BN) with a doping ratio of 0%–100%. They found that when the doping concentration was 50% with a h-BN size of 2 nm, the *k* of composite structure could be reduced by 65%. However, to our best knowledge, the investigation of the thermal conductivity in monolayer C$_3$B$_x$N$_{1-x}$ alloy is still blank. Therefore, the exploration on this subject is urgent.

In this study, we use the MD method to evaluate the thermal properties of monolayer C$_3$B$_x$N$_{1-x}$ alloy. At first, we calculate *k* of monolayer C$_3$B$_x$N$_{1-x}$ alloy as a function of
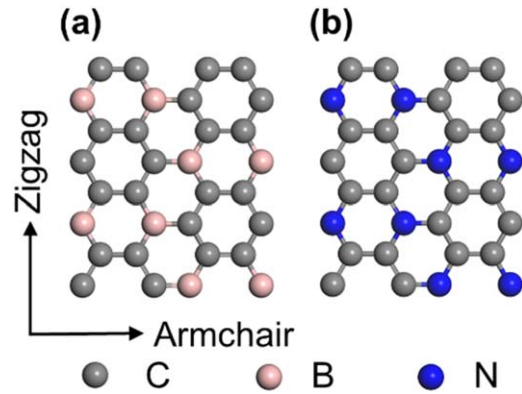

Figure 1. Atomic configurations of monolayer (a) C$_3$B and (b) C$_3$N.

random doping ratio (*x*). Afterwards, we evaluate the spatiotemporal thermal transport, phonon group velocity, participation ratio (PR) and phonon wave packet simulations in monolayer C$_3$B$_x$N$_{1-x}$ alloy to analyze the phonon behaviors. Furthermore, we fix *x* at 0.5 to investigate the thermal conductivity of the superlattice (C$_3$B$_{0.5}$N$_{0.5}$-SL), which can be considered as the special alloy. Then the variation of *k* with the increase of period length is presented. The phonon density of states (PDOS), phonon group velocity, PR and phonon wave packet simulation are also calculated to uncover the underlying phonon transport mechanism in C$_3$B$_{0.5}$N$_{0.5}$-SL.

2. Simulation details

In this study, all MD simulations are performed using the Large-scale Atomic/Molecular Massively Parallel Simulator (LAMMPS) package [25]. The optimized Tersoff potentials by Lindsay and Broido [26] for C–C atomic interactions and by Kinarci [27] for C–N and C–B atomic interactions in monolayer C$_3$B$_x$N$_{1-x}$ alloy have been selected, which can predict thermal properties and the phonon dispersion curves in some 2D structures [28–31]. Here we adopt this potential to model the C–C, C–B and C–N interactions within the monolayer C$_3$B$_x$N$_{1-x}$ alloy. Atomic configurations of the monolayer C$_3$B and C$_3$N are shown in figure 1, which possess two different directions (armchair and zigzag directions). In our simulation, the armchair and zigzag directions are along the *x* and *y* directions, respectively. Owing to the negligible effects of chirality on C$_3$B and C$_3$N [20], we only calculate the thermal conduction along the armchair direction.

For MD simulations, periodic boundary conditions are used in all three directions. The large vacuum layer of 10 nm along *z* direction is set to avoid the atomic interaction with the system image. The timestep for all MD simulations is 0.5 fs. We first place the system in the isothermal-isobaric ensemble (NPT) at 0 bar for 500 ps and then in the canonical ensemble (NVT) for 500 ps to relax the system structure until the equilibrium. The above relaxation processes are controlled at 300 K. The system is then switched to the micro-canonical ensemble (NVE) for 500 ps. Thereafter, we conduct the non-equilibrium molecular dynamics (NEMD) simulation under
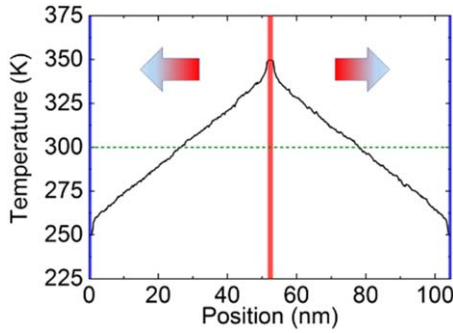
Figure 2. Steady temperature distribution of monolayer $C_3B_{0.5}N_{0.5}$ in the NEMD simulation.

NVE for 6 ns [32]. As shown in figure 2, the middle region (red) and outermost regions (blue) are set as the heat source with 2 nm and two heat sinks with 2 nm, respectively. The Langevin thermostats are utilized to control the temperature of heat source (350 K) and heat sinks (250 K). After first 5 ns, the system arrives at the steady state and obtains a stable temperature gradient. Sequentially, the last 1 ns of the NEMD process is used to record the kinetic energies of all atoms. According to energy equipartition theorem, we can calculate the temperature distribution of the system. To obtain the temperature profile along the *x* direction, we evenly divide the system into *n* slabs with a slab length of 0.2 nm. Afterwards, the thermal conductivity can be evaluated by the Fourier's law of heat conduction:

$$Q = -A \cdot k \frac{\partial T}{\partial x}, \qquad (1)$$

where Q is heat flux, A represents the cross-sectional area of the heat flux, T represents the temperature, x represents the direction of heat flux, and k is the thermal conductivity. Because the thickness of monolayers C_3B and C_3N are 3.3 Å [13] and 3.2 Å [33], respectively, we choose the average thickness (3.25 Å) as the thickness of monolayer $C_3B_xN_{1-x}$ alloy. In order to suppress the statistical error, we perform five independent simulations with different initial conditions for all simulations. The final thermal conductivity value is the average of the five results with the standard deviations shown as error bars.

3. Results and discussions

### 3.1. Monolayer $C_3B_xN_{1-x}$ alloy by random doping

The monolayer $C_3B_xN_{1-x}$ alloy is designed by random doping the B atoms embedded with monolayer C_3N as shown in figure 3(a), where the range of *x* is from 0 to 1.0. The system size of the monolayers is selected as 102.26×4.92 nm². Figure 3(b) shows the variational thermal conductivity with the increasing parameter *x*. When *x* is equal to 0, the structure is pure C_3N, and the calculated thermal conductivity is 547.67 W m⁻¹ K⁻¹. As *x* becomes 1.0, the structure turns to pure C_3B, and we calculate the *k* as 346.73 W m⁻¹ K⁻¹. The thermal conductivity results of pure C_3N and C_3B are similar
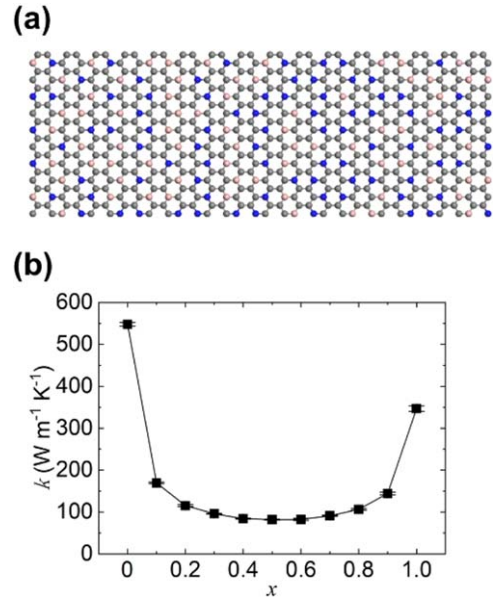
Figure 3. (a) Atomic configuration of monolayer $C_3B_{0.5}N_{0.5}$. (b) Thermal conductivities of monolayer $C_3B_xN_{1-x}$ alloy with *x* ranging from 0 to 1.0.

to the previous work done by Song *et al* [20]. They found that the *k* of C_3N and C_3B with a similar length to our work were ~509.92 and ~305.15 W m⁻¹ K⁻¹. The phonon lifetime of flexural acoustic (ZA) mode in graphene with N atoms doping is larger than B atoms doping because of the similar mass perturbations between C and N atoms [34], which leads to larger thermal conductivity in monolayer C_3N. It should be noted that the curve in figure 3(b) shows a U-shaped variation, which is similar to other studies [35, 36]. When $x < 0.5$, B atoms can be considered as impurity in monolayer C_3N, which act as the scattering cores to reduce the thermal conductivity. The thermal transport in monolayer $C_3B_xN_{1-x}$ will be obstructed by the impurity because of the phonon-impurity scattering. As the *x* enhances, the number of impurity atoms increases and the phonon-impurity scattering is elevated. Therefore, the thermal conductivity of monolayer $C_3B_xN_{1-x}$ alloy is reduced until *x* equal 0.5, and the lowest thermal conductivity is 81.78 W m⁻¹ K⁻¹. However, when $x > 0.5$, the N atoms become dopants in monolayer $C_3B_xN_{1-x}$, which causes the increasing *k* in the monolayer alloy. We note that the range of *x* majorly locates below 0.2 and above 0.8 with the drastically variation of thermal conductivity, which could be ascribed to the localization of phonon modes. This phenomenon is consistent with the previous work [36]. By doping germanium atoms into silicene nanosheets, Wang *et al* [36] found the nanosheets possessed lower thermal conductivity due to the enhancive phonon-impurity scattering. The variation trend of thermal conductivity with doping ratio is also a U-shaped profile, and the lowest *k* corresponding to the doping ratio is 50%.

For sake of comparing the heat dissipation in monolayer $C_3B_xN_{1-x}$ alloy intuitively, we calculate and analyze the spatiotemporal thermal transport simultaneously. After the system reaches thermal equilibrium, we impose a high heat
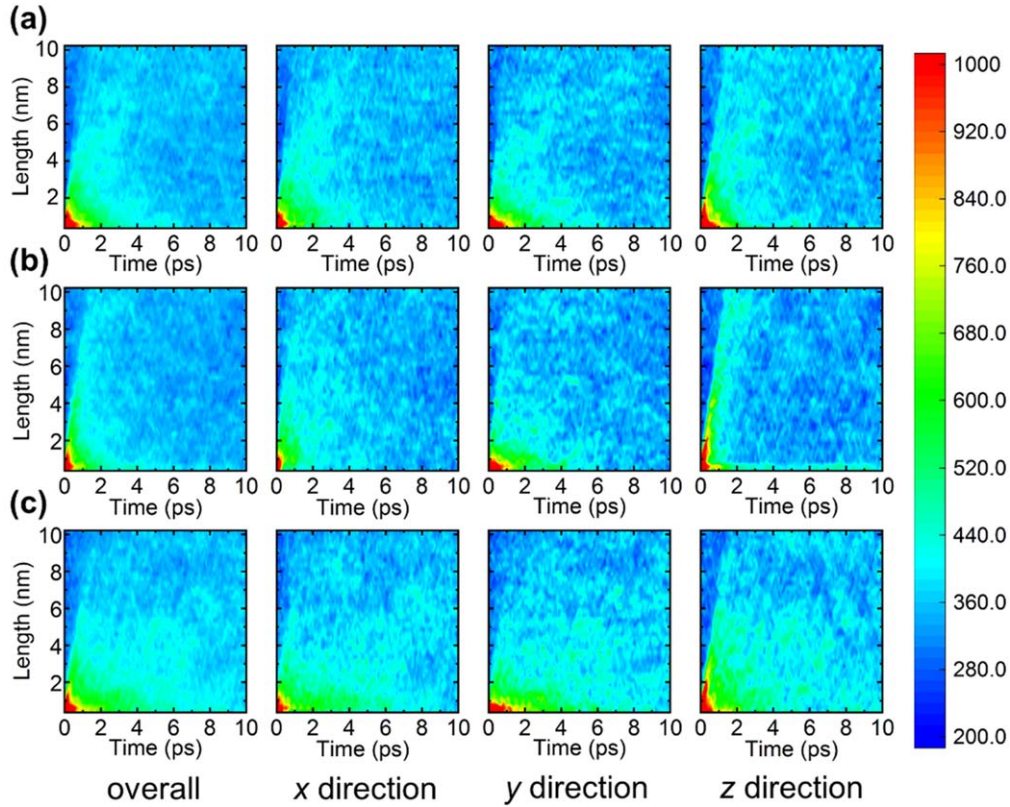
Figure 4. Spatiotemporal thermal maps through (a) C_3B, (b) C_3N, and (c) $C_3B_{0.5}N_{0.5}$ in overall, *x* direction, *y* direction and *z* direction, respectively. The color bars represent temperature in a unit of K.

impulse of 9×10^{13} W m^{-2} for 50 fs at 0.5 nm × 4.92 nm region of left side in monolayer for C_3B, C_3N and $C_3B_{0.5}N_{0.5}$. The local thermal energy will dissipate by spreading to the whole system until the system re-reaches the thermal equilibrium. Figures 4(a)–(c) show the spatiotemporal thermal transport of C_3B, C_3N and $C_3B_{0.5}N_{0.5}$ in overall, *x* direction, *y* direction and *z* direction, respectively. We can observe two phenomena from the results: (1) The temperature of C_3N drops faster than others, in which the heat dissipation in monolayer $C_3B_{0.5}N_{0.5}$ takes much longer time. The results further confirm the thermal conductivities we calculate. (2) The ZA phonon modes carry much more energy than other two acoustic phonon modes in all three structures [34]. Hence, the ZA phonon modes make the major contribution to the thermal conductivity of graphene derivative monolayers.

In order to uncover phonon transport mechanisms of monolayer $C_3B_xN_{1-x}$ alloy, we calculate the phonon group velocities and PRs of C_3B, C_3N and $C_3B_{0.5}N_{0.5}$ with 960 atoms by using lattice dynamics (LD) simulation. All LD simulations are performed with General Utility Lattice Program (GULP) package [37]. First, we calculate the phonon group velocity to analyze the capacity of phonon thermal transport in monolayers. Figure 5 shows the relation between phonon group velocity and phonon frequency. The highest phonon group velocity of C_3B and C_3N are as high as 19.97 and 20.92 km s^{-1}, which consist with other works [38, 39] (C_3B: ∼20.18 km s^{-1} and C_3N: ∼22.07 km s^{-1}), respectively. In order to make a more visual comparison, we calculate the average phonon group velocity. The average phonon group

velocities of C_3B, C_3N and $C_3B_{0.5}N_{0.5}$ are 2.95 km s^{-1}, 3.51 km s^{-1} and 0.99 km s^{-1}, respectively. It can be observed that monolayer $C_3B_{0.5}N_{0.5}$ alloy possesses the lowest phonon group velocity in all three materials. Therefore, the reduction of phonon group velocity in the alloy hinders thermal energy transmission, which can confirm our MD simulation results.

Afterwards, the PR is further calculated to evaluate the localization of monolayer alloy phonon modes with the following formula [40]:

$$P_\lambda^{-1} = N \sum_{i=1}^{N} \left(\sum_{\alpha=1}^{3} e_{i\alpha,\lambda}^* e_{i\alpha,\lambda} \right)^2, \qquad (2)$$

where, N is the total number of atoms, $e_{i\alpha,\lambda}$ means the eigenvector with λth polarization from α direction of ith atom in the lattice, and α represents x, y and z directions. The PR can describe the ratio of the atoms participation in the motion [41]. When PR equals 1.0, it means all atoms take part in the eigen-vibration and the phonon modes are non-localized, which manifests that the phonons are able to transport in the whole system. However, for the small PR, some scattering (phonon-impurity scattering and phonon-boundary scattering) in the system can lead to some phonon modes localization, which impedes the phonon spreading in the whole system. As shown in figure 6, monolayer C_3N has the highest PR in the whole frequency region, monolayer $C_3B_{0.5}N_{0.5}$ possesses the lowest PR, and monolayer C_3B falls in between them. The average PRs of C_3B, C_3N and $C_3B_{0.5}N_{0.5}$ are 0.69, 0.71 and 0.45, respectively. We can deduce that there are more
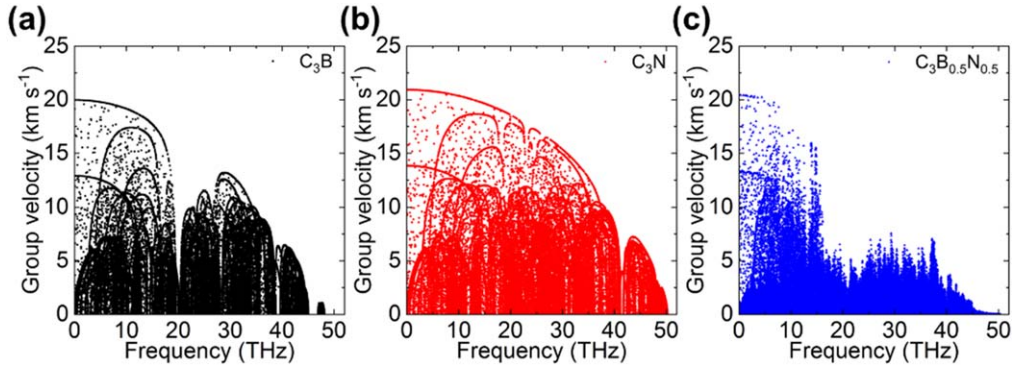
Figure 5. Phonon group velocities of (a) C_3B, (b) C_3N and (c) $C_3B_{0.5}N_{0.5}$ calculated from lattice dynamics using GULP.
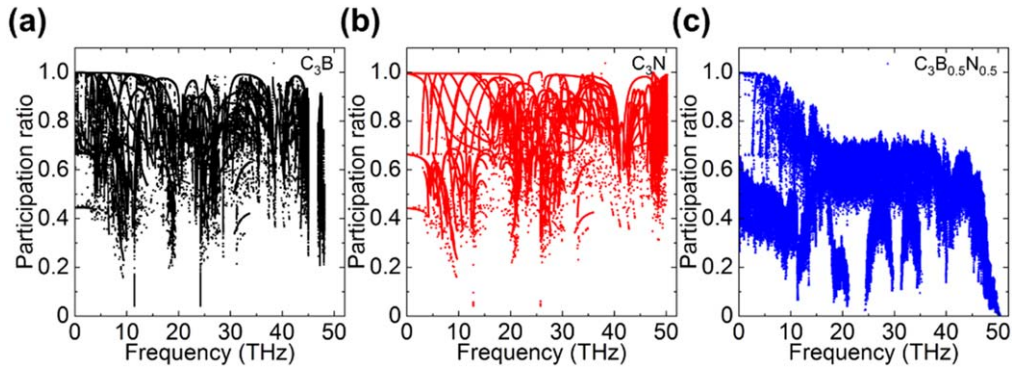
Figure 6. Phonon participation ratios of (a) C_3B, (b) C_3N and (c) $C_3B_{0.5}N_{0.5}$ calculated from lattice dynamics using GULP.

localized phonon modes in monolayer $C_3B_{0.5}N_{0.5}$ due to the strong phonon-impurity scattering. For the $C_3B_{0.5}N_{0.5}$ alloy, the doping atoms generate the different edge configurations, *i.e.* different edge atoms, which enhances the phonon localization in alloy system [42]. According to the above phonon group velocity and PR analyses, we can obtain two conclusions: (1) Due to the reduction of the phonon group velocities, the phonon transmission is hindered, which results in the reduction of the k of monolayer $C_3B_xN_{1-x}$ alloy. (2) Due to the heterogeneous atoms, there are more localized phonon edge modes in $C_3B_{0.5}N_{0.5}$ than others, which can suppress the k of $C_3B_{0.5}N_{0.5}$.

As we mention above, the phonon-impurity scatterings induce the reduction of thermal conductivity. In order to further get insight into the underlying phonon transmission essence, the phonon wave packet simulations are conducted [43, 44]. The principle of phonon wave packet simulation focuses on revealing the wave packet behaviors cross the interface. Here the phonon wave packet simulations are performed under 0 K. To avoid the mutual influence of the phonon wave packet movement along the direction [45], the size of structure is choose as 1000 nm. In this study, we choose C_3B as the original material to excite the phonon wave packet, and the length ratio of the pristine C_3B and $C_3B_xN_{1-x}$ is 1:1. Periodic boundary conditions are adopted along all three directions, and the thickness of vacuum layer is still 10 nm. After fully relaxing the system at 0 K via the energy minimization using conjugate gradient (CG) algorithm, we apply the original phonon wave packet according to the

formula [43]:

$$u_{il,\lambda} = Me_{i\alpha,\lambda}(k_0)\exp\left[ik_0(x_l - x_0)\right]$$
$$\times \exp[-(x_l - x_0)^2/\sigma^2] \quad (3)$$

$$v_{il,\lambda} = -i\omega_\lambda u_{il,\lambda}, \quad (4)$$

where, $u_{il,\lambda}$ represents the λth component of displacement for ith atom in lth unit cell, α represents the direction of eigenmode, and k_0 means the wavevector, v represents the initial velocity of phonon wave packet. The eigenvector and wavevector in the equations can be chosen and calculated by LD simulations [46]. In this section, we conduct three structures: C_3B-C_3B, C_3B-C_3N and C_3B-$C_3B_{0.5}N_{0.5}$. To generate the original phonon wave packet of the longitude acoustic (LA) phonon mode, the wavevector k_0 is selected as $0.05 \times (2\pi/a)$, where the a is the lattice constant, the corresponding frequency of k_0 is 2.29 THz and the amplitude of wave (M) is chosen as 0.01 Å.

The launch and propagation of wave packets in three structures are shown in figure 7. The same phonon wave packets move in the x direction. When the time is equal to 6 ps, the wave packets cross the interface, and then continue moving along the x direction. We can observe that there is no deformation in C_3B-C_3B because of the negligible anharmonic phonon scattering in figure 7(a), which indicates that the wave packet propagates ballistically. However, the pristine wave packets in C_3B-C_3N and C_3B-$C_3B_{0.5}N_{0.5}$ are separated into two parts (the transmitted wave and the reflected wave). We attribute this phenomenon to different phonon modes in
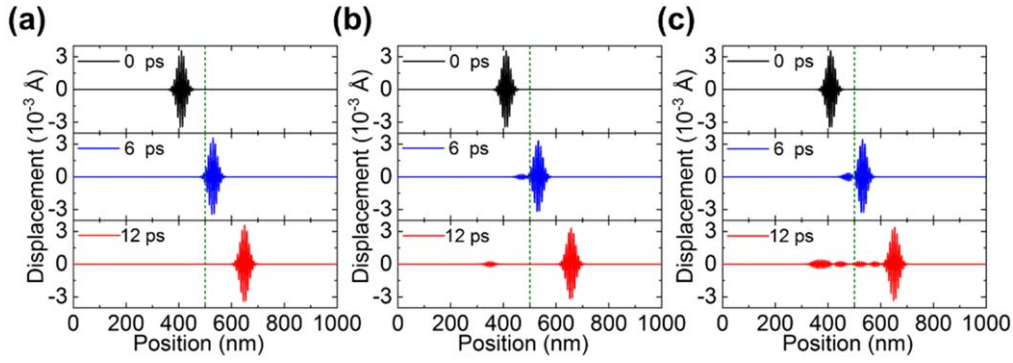
Figure 7. The propagation of the phonon wave packet in (a) C_3B-C_3B, (b) C_3B-C_3N and (c) C_3B-$C_3B_{0.5}N_{0.5}$ at 0 ps, 6 ps and 12 ps. The dotted line is the interface between C_3B and C_3B (or C_3N or $C_3B_{0.5}N_{0.5}$).
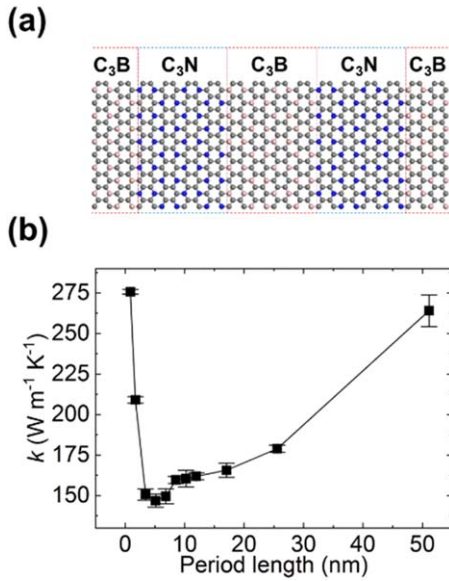
Figure 8. (a) Atomic configuration of monolayer $C_3B_{0.5}N_{0.5}$-SL. (b) Thermal conductivities of monolayer $C_3B_{0.5}N_{0.5}$-SL at different period lengths.

different material parts. At 12 ps, the transmitted wave and the reflected wave in C_3B-C_3N system continue move along the positive and negative x directions, respectively (figure 7(b)). Nevertheless, the continuous reflected waves in C_3B-$C_3B_{0.5}N_{0.5}$ system have been observed in figure 7(c). The random doping atoms in $C_3B_{0.5}N_{0.5}$ part generate the consecutive phonon-impurity scatterings, which leads to the appearance of new reflected waves. The results of phonon wave packet simulation further confirm the phonon trans-mission behaviors which we discuss above.

3.2. Monolayer C_3B-C_3N superlattice

Superlattice is the special alloy with the periodic hybrid material structure. It possesses the repeating units in a certain period length (l_p), which can be utilized in thermoelectric devices [47–50]. We fix the parameter x at 0.5 to construct C_3B-C_3N superlattice ($C_3B_{0.5}N_{0.5}$-SL). The atomic structure of $C_3B_{0.5}N_{0.5}$-SL is shown in figure 8(a). The length of $C_3B_{0.5}N_{0.5}$-SL is the same as that of the system with the random doping (102.26 nm). The period length is ranged

between 0.85 and 51.13 nm. Figure 8(b) shows the relation-ship between the thermal conductivity and the period length. When the period length increases, the thermal conductivity first decreases and reaches minimum (145.32 W m^{-1} K^{-1}) at $l_p = 5.11$ nm, then the thermal conductivity further enhances. The trend of the k is consistent with the other research [36]. In general, the corresponding period length of the lowest k is known as the coherent length, which is 5.11 nm in our work. When the period length is smaller than coherent length, it is the coherent region, and when the period length is larger than coherent length, it is called the incoherent region.

For sake of presenting the vibration of the phonons in different frequency, we calculate the PDOS of C_3B and C_3N parts in the $C_3B_{0.5}N_{0.5}$-SL by taking the Fourier transform of the velocity autocorrelation function:

$$F(\omega) = \frac{1}{\sqrt{2\pi}} \int_{-\infty}^{\infty} e^{-i\omega t} \frac{\langle v(t) \cdot v(0) \rangle}{\langle v(0) \cdot v(0) \rangle} dt, \qquad (5)$$

where, $F(\omega)$ represents the PDOS at ω angular frequency, $v(t)$ and $v(0)$ represent the atom velocity vectors at the time of t and 0, respectively. The PDOS of C_3B and C_3N parts in the $C_3B_{0.5}N_{0.5}$-SL with 0.85 nm, 5.11 nm and 10.23 nm are shown in figures 9(a)–(c), respectively. The PDOS of C_3B and C_3N parts at the low frequency region is analogous in all three monolayers. However, in medium and high frequency regions, we can observe the diversities between the two parts with the increase of period length. Especially, the G-band of C_3B part shows the red-shift while that of C_3N part shifts to the higher frequency when the period length increases. To make a more visual comparison, we calculate the overlapping factor (S) by the follow equation [51, 52]:

$$S = \frac{\int_{-\infty}^{\infty} F_1(\omega) \cdot F_2(\omega) d\omega}{\int_{-\infty}^{\infty} F_1(\omega) d\omega \cdot \int_{-\infty}^{\infty} F_2(\omega) d\omega}, \qquad (6)$$

where subscripts '1' and '2' represent phonon modes of C_3B and C_3N parts, respectively. The overlapping factors of superlattice with period length of 0.85 nm, 5.11 nm and 10.23 nm are 0.0240, 0.0226 and 0.0214, which verifies that the difference of lattice vibrations in C_3B and C_3N parts become more distinct when the period length enhances.
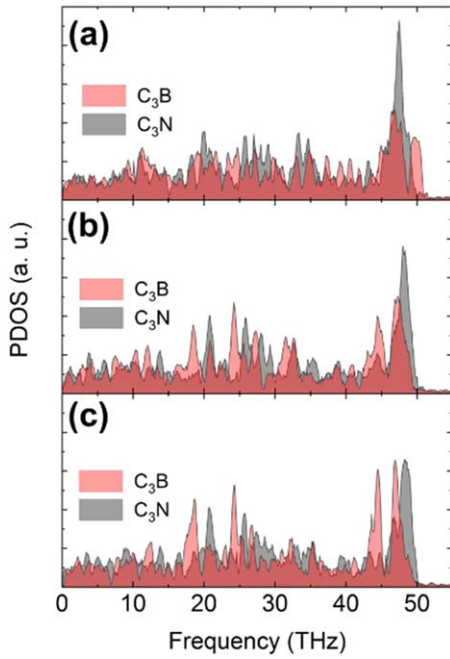
Figure 9. Phonon density of states (PDOS) for $C_3B_{0.5}N_{0.5}$-SL with period length of (a) 0.85 nm, (b) 5.11 nm and (c) 10.23 nm.

According to the previous studies [53, 54], the phonon transport of superlattice shows wave and particle properties in coherent and incoherent regions, respectively. In the coherent region, the phonon modes in C_3B and C_3N parts show an interference phenomenon because the wavelength of phonon is larger than the period length. The incident and reflected phonons at the interface of superlattice form the coherent phonon modes, which induces that the phonon-interface scattering will not happened at the inner interface of a period. Hence the whole material can be considered as a 'newly generated material' [36]. According to the PDOS results, the overlapping factor is higher when $l_p = 0.85$ nm, but reduces when the period length increases to 5.11 nm. We further calculate the phonon group velocities and PRs of $C_3B_{0.5}N_{0.5}$-SL in coherent region with the period length of 0.85 nm, 1.70 nm and 5.11 nm in figures 10(a)–(c) and 11(a)–(c), respectively. The average phonon group velocities of $C_3B_{0.5}N_{0.5}$-SL with the period length of 0.85 nm, 1.70 nm and 5.11 nm are 2.59 km s^{-1}, 2.34 km s^{-1} and 1.86 km s^{-1}, and the corresponding PRs are 0.59, 0.56 and 0.45, respectively. Hence, the decreasing phonon group velocity and PR demonstrates that the phonon transmission of $C_3B_{0.5}N_{0.5}$-SL for the higher period length in coherent region is hindered, so the thermal conductivity will reduce. On the other hand, when the period length is larger than coherent length, the particle nature of the phonon plays a dominant role in the energy transport. Phonons will not skip the interface directly, and the phonon-interface scattering will cannot be ignored. Nevertheless, with the increase of the period length, the number of the interface in superlattice decreases, which lessens the phonon scattering, and the thermal conductivity will bounce back to a larger value.

To observe the phonon scattering at the inner interface in monolayer $C_3B_{0.5}N_{0.5}$-SL, we also conduct the phonon wave packet simulations. The simulation parameters are same as the
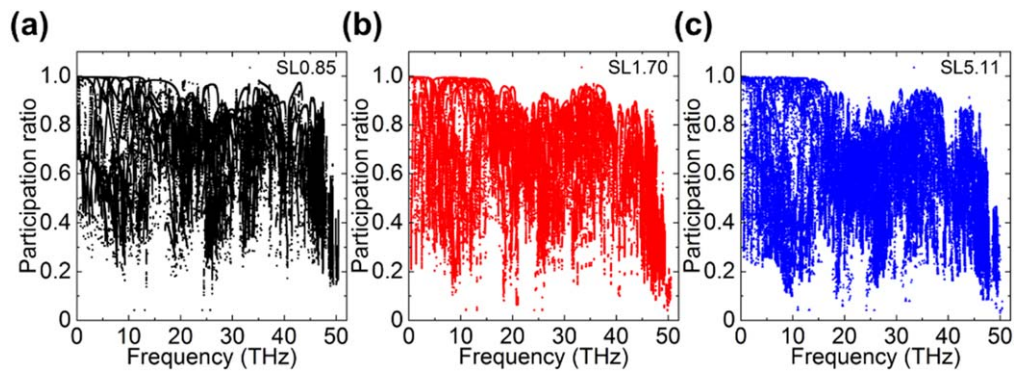
phonon wave packet simulation of figure 7. Figure 12 shows the phonon wave packet behaviors in C_3B and $C_3B_{0.5}N_{0.5}$-SL with the period length of 0.85 nm, 5.11 nm and 10.23 nm, respectively. In C_3B-SL0.85 system, the initial phonon-interface scattering happens at 6 ps, which generates the transmitted wave and the reflected wave. Afterwards, the two parts propagate along the positive and negative x direction, respectively. This phenomenon proves that the superlattice in coherent region can be considered as a 'newly generated material', which is similar to the result of C_3B-C_3N as shown in figure 7(b). When the phonon wave packet steps over the interface in C_3B-SL5.11 system, the transmitted wave packet deforms. At 12 ps, the wave packet in the superlattice part is continuously reflected by the inner interface of the superlattice. For the C_3B-SL10.23, the consecutively reflection of phonon wave can also exist, but the reflection intensity get weaker in comparison with C_3B-SL5.11, which confirms that the phonon-interface scattering is alleviated. On the basis of the results of the phonon wave simulation, we can vividly prove the phonon behaviors in the superlattice with different period lengths, which further reveals the non-monotonic variation of thermal conductivity in figure 8(b).

4. Conclusions

In this work, we use the MD simulations to evaluate the thermal properties of monolayer $C_3B_xN_{1-x}$ alloy. The thermal conductivity of monolayer $C_3B_xN_{1-x}$ alloy presents a U-shaped profile with the increase of random doping ratio (x). The k arrives the minimum at $x = 0.5$, which is equal to 81.78 W m^{-1} K^{-1}. We analyze the phonon behaviors in monolayer $C_3B_xN_{1-x}$ alloy via calculating the phonon group velocity, PR and phonon wave packet simulations of monolayer $C_3B_xN_{1-x}$ alloy. In monolayer $C_3B_{0.5}N_{0.5}$ alloy, the phonon group velocity and PR are much smaller than those in pure C_3B and C_3N due to the enhancive phonon-impurity scatterings. Moreover, we can observe the continuous reflected waves in C_3B-$C_3B_{0.5}N_{0.5}$ system by using phonon wave packet simulation. The appearance of new reflected waves can be attributed to the consecutive phonon-impurity scatterings in $C_3B_{0.5}N_{0.5}$. Afterwards, we fix x as 0.5 to evaluate the thermal conductivity of monolayer $C_3B_{0.5}N_{0.5}$-SL, which shows an initial decreasing and then rising trend. The minimum thermal conductivity value is 146.85 W m^{-1} K^{-1}, and the corresponding period length is 5.11 nm which is also called coherent length. When the period length is smaller than the coherent length, the average phonon group velocities and PRs in monolayer $C_3B_{0.5}N_{0.5}$-SL decrease monotonically as the period length increases from 0.85 to 5.11 nm, which can demonstrate that the phonon transport capacity of $C_3B_{0.5}N_{0.5}$-SL for the higher period length in coherent region is lessened, so the thermal conductivity will reduce. Moreover, the results of PDOS and phonon wave packet simulation can prove that the superlattice can be considered as a 'newly generated material' in coherent region. In incoherent region, the thermal conductivity will enhance on account of the decreasing number of the interface in superlattice and the lessened phonon-interface scattering, which can be verified by phonon wave packet simulation. Our work is expected to
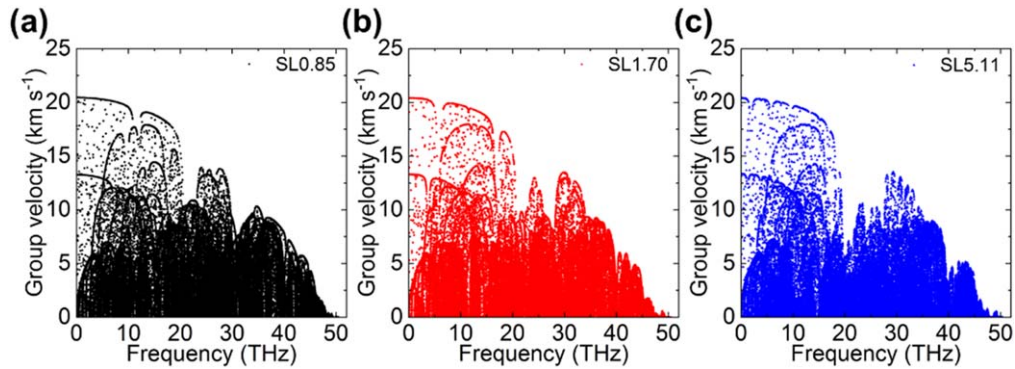
Figure 10. Phonon group velocities of $C_3B_{0.5}N_{0.5}$-SL with period length of (a) 0.85 nm, (b) 1.70 nm and (c) 5.11 nm calculated from lattice dynamics using GULP.

Figure 11. Phonon participation ratios of $C_3B_{0.5}N_{0.5}$-SL with period length of (a) 0.85 nm, (b) 1.70 nm and (c) 5.11 nm calculated from lattice dynamics using GULP.
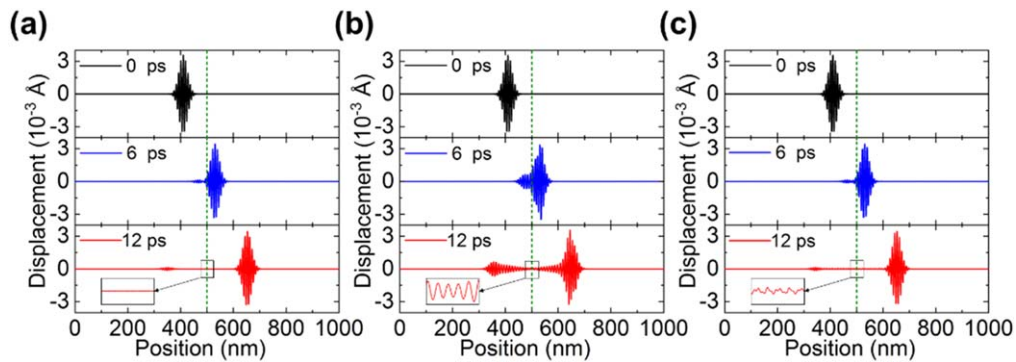
Figure 12. The propagation of the phonon wave packet in the C_3B-$C_3B_{0.5}N_{0.5}$-SL with period length of 0.85, 5.11 and 10.23 nm at 0 ps, 6 ps and 12 ps. The dotted line is the interface between C_3B and superlattice. The insets are the zoom-in pictures of black boxes at the interfaces in the C_3B-$C_3B_{0.5}N_{0.5}$-SL.

provide a fundamental physical guideline to tune the thermal transport of 2D materials.

Conflicts of interest

There are no conflicts of interest to declare.

ORCID iDs

Xinyu Wang ⓘ https://orcid.org/0000-0003-4143-334X
Qian Xin ⓘ https://orcid.org/0000-0003-4605-5894
Gongming Xin ⓘ https://orcid.org/0000-0003-3974-0391

References

[1] Xu X *et al* 2014 Length-dependent thermal conductivity in suspended single-layer graphene *Nat. Commun.* **5** 3689

[2] Ni Z, Liu Q, Tang K, Zheng J, Zhou J, Qin R, Gao Z, Yu D and Lu J 2012 Tunable bandgap in silicene and germanene *Nano Lett.* **12** 113–8

[3] Hao F, Fang D and Xu Z 2011 Mechanical and thermal transport properties of graphene with defects *Appl. Phys. Lett.* **99** 041901

[4] Singh A K and Yakobson B I 2009 Electronics and magnetism of patterned graphene nanoroads *Nano Lett.* **9** 1540–3

[5] Xu X, Chen J and Li B 2016 Phonon thermal conduction in novel 2D materials *J. Phys.-Condens. Matter* **28** 483001

[6] Novoselov K S, Geim A K, Morozov S V, Jiang D, Zhang Y, Dubonos S V, Grigorieva I V and Firsov A A 2004 Electric field effect in atomically thin carbon films *Science* **306** 666–9

[7] Balandin A A, Ghosh S, Bao W, Calizo I, Teweldebrhan D, Miao F and Lau C N 2008 Superior thermal conductivity of single-layer graphene *Nano Lett.* **8** 902–7

[8] Miller J R, Outlaw R A and Holloway B C 2011 Graphene electric double layer capacitor with ultra-high-power performance *Electrochim. Acta* **56** 10443–9

[9] Özyilmaz B, Jarillo-Herrero P, Efetov D, Abanin D A, Levitov L S and Kim P 2007 Electronic transport and quantum hall effect in bipolar graphene *p-n-p* junctions *Phys. Rev. Lett.* **99** 166804

[10] Yanagisawa H, Tanaka T, Ishida Y, Matsue M, Rokuta E, Otani S and Oshima C 2004 Phonon dispersion curves of a BC$_3$ honeycomb epitaxial sheet *Phys. Rev. Lett.* **93** 177003

[11] Yang S *et al* 2017 C$_3$N-a 2D crystalline, hole-free, tunable-narrow-bandgap semiconductor with ferromagnetic properties *Adv. Mater.* **29** 1605625

[12] Chen J, Cheng X L and Zhang H 2019 Plasmon excitation in BC$_3$ nanostructures from first principles *Plasmonics* **14** 109–16

[13] Li S-S, Zhang C-W, Ji W-X, Li F and Wang P-J 2014 Tunable electronic properties induced by a defect-substrate in graphene/BC$_3$ heterobilayers *Phys. Chem. Chem. Phys.* **16** 22861–6

[14] Ren Y, Cheng F, Zhou X, Chang K and Zhou G 2019 Tunable mechanical, electronic and magnetic properties of monolayer C$_3$N nanoribbons by external fields *Carbon* **143** 14–20

[15] Rani S and Ray S J 2019 Detection of gas molecule using C$_3$N island single electron transistor *Carbon* **144** 235–40

[16] Wu T, Shen H, Lei S, Cheng B, Liu B and Shen J 2012 Nitrogen and boron doped monolayer graphene by chemical vapor deposition using polystyrene, urea and boric acid *New J. Chem.* **36** 1385–91

[17] Liu X B, Ma X, Gao H, Zhang X, Ai H, Li W and Zhao M 2018 Valley-selective circular dichroism and high carrier mobility of graphene-like BC$_6$N *Nanoscale* **10** 13179–86

[18] Hua Y, Li H and Cao B 2019 Thermal spreading resistance in ballistic-diffusive regime for GaN HEMTs *IEEE Trans. Electron Devices* **66** 3296–301

[19] Xu Y, Li Z and Duan W 2014 Thermal and thermoelectric properties of graphene *Small* **10** 2182–99

[20] Song J, Xu Z, He X, Bai Y, Miao L, Cai C and Wang R 2019 Thermal conductivity of two-dimensional BC$_3$: a comparative study with two-dimensional C$_3$N *Phys. Chem. Chem. Phys.* **21** 12977–85

[21] Hong Y, Zhang J and Zeng X C 2018 Monolayer and bilayer polyaniline C$_3$N: two-dimensional semiconductors with high thermal conductivity *Nanoscale* **10** 4301

[22] Mortazavi B and Ahzi S 2012 Molecular dynamics study on the thermal conductivity and mechanical properties of boron doped graphene *Solid State Commun.* **152** 1503–7

[23] Goharshadi E K and Mahdizadeh S J 2015 Thermal conductivity and heat transport properties of nitrogen-doped graphene *J. Mol. Graphics Modell.* **62** 74–80

[24] Wang J, Mu X, Wang X, Wang N, Ma F, Liang W and Sun M 2018 The thermal and thermoelectric properties of in-plane C-BN hybrid structures and graphene/h-BN van der Waals heterostructures *Mater. Today* **5** 29–57

[25] Plimpton S 1995 Fast parallel algorithms for short-range molecular-dynamics *J. Comput. Phys.* **117** 1–19

[26] Lindsay L and Broido D A 2010 Optimized Tersoff and Brenner empirical potential parameters for lattice dynamics and phonon thermal transport in carbon nanotubes and graphene *Phys. Rev.* B **81** 205441

[27] Kinaci A, Haskins J B, Sevik C and Cagin T 2012 Thermal conductivity of BN-C nanostructures *Phys. Rev.* B **86** 115410

[28] Lindsay L, Li W, Carrete J, Mingo N, Broido D A and Reinecke T L 2014 Phonon thermal transport in strained and unstrained graphene from first principles *Phys. Rev.* B **89** 155426

[29] Shirazi A H N, Abadi R, Izadifar M, Alajlan N and Rabczuk T 2018 Mechanical responses of pristine and defective C$_3$N nanosheets studied by molecular dynamics simulations *Comput. Mater. Sci.* **147** 316–21

[30] Zahedi R K, Shirazi A H N, Alimouri P, Alajlan N and Rabczuk T 2019 Mechanical properties of graphene-like BC$_3$; a molecular dynamics study *Comput. Mater. Sci.* **168** 1–10

[31] Wang X, Wang M, Hong Y, Wang Z and Zhang J 2017 Coherent and incoherent phonon transport in a graphene and nitrogenated holey graphene superlattice *Phys. Chem. Chem. Phys.* **19** 24240

[32] Bao H, Chen J, X G and B C 2018 A review of simulation methods in micro/nanoscale heat conduction *ES Energy Environ.* **1** 16–55

[33] Mortazavi B 2017 Ultra high stiffness and thermal conductivity of graphene like C$_3$N *Carbon* **118** 25–34

[34] Polanco C A and Lindsay L 2018 *Ab initio* phonon point defect scattering and thermal transport in graphene *Phys. Rev.* B **97** 014303

[35] Xu R-F, Han K and Li H-P 2018 Effect of isotope doping on phonon thermal conductivity of silicene nanoribbons: a molecular dynamics study *Chin. Phys.* B **27** 026801

[36] Wang X, Hong Y, Chan P K L and Zhang J 2017 Phonon thermal transport in silicene-germanene superlattice: a molecular dynamics study *Nanotechnology* **28** 255403

[37] Gale J D 1997 GULP: a computer program for the symmetry-adapted simulation of solids *J. Chem. Soc.-Faraday Trans.* **93** 629–37

[38] Mortazavi B, Shahrokhi M, Raeisi M, Zhuang X, Pereira L F C and Rabczuk T 2019 Outstanding strength, optical characteristics and thermal conductivity of graphene-like BC$_3$ and BC$_6$N semiconductors *Carbon* **149** 733–42

[39] Gao Y, Wang H, Sun M, Ding Y, Zhang L and Li Q 2018 First-principles study of intrinsic phononic thermal transport in monolayer C$_3$N *Physica* E **99** 194–201

[40] Bodapati A, Schelling P K, Phillpot S R and Keblinski P 2006 Vibrations and thermal transport in nanocrystalline silicon *Phys. Rev.* B **74** 245207

[41] Monthus C and Garel T 2010 Anderson localization of phonons in dimension $d = 1, 2, 3$: finite-size properties of the inverse participation ratios of eigenstates *Phys. Rev.* B **81** 224208

[42] Jiang J-W, Lan J, Wang J-S and Li B 2010 Isotopic effects on the thermal conductivity of graphene nanoribbons: localization mechanism *J. Appl. Phys.* **107** 054314

[43] Schelling P K, Phillpot S R and Keblinski P 2002 Phonon wave-packet dynamics at semiconductor interfaces by molecular-dynamics simulation *Appl. Phys. Lett.* **80** 2484–6

[44] Hu S, Zhang Z, Jiang P, Ren W, Yu C, Shiomi J and Chen J 2019 Disorder limits the coherent phonon transport in two-dimensional phononic crystal structures *Nanoscale* **11** 11839–46

[45] Shi J, Lee J, Dong Y, Roy A, Fisher T S and Ruan X 2018 Dominant phonon polarization conversion across dimensionally mismatched interfaces: carbon-nanotube-graphene junction *Phys. Rev.* B **97** 134309

[46] Shao C, Rong Q, Li N and Bao H 2018 Understanding the mechanism of diffuse phonon scattering at disordered surfaces by atomistic wave-packet investigation *Phys. Rev.* B **98** 155418

[47] Jia T T, Zheng M M, Fan X Y, Su Y, Li S J, Liu H Y, Chen G and Kawazoe Y 2015 Band gap on/off switching of silicene superlattice *J. Phys. Chem.* C **119** 20747–54

[48] Luckyanova M N, Johnson J A, Maznev A A, Garg J, Adam J, Bulsara M T, Fitzgerald E A, Nelson K A and Chen G 2013 Anisotropy of the thermal conductivity in GaAs/AlAs superlattices *Nano Lett.* **13** 3973–7

[49] Lee S M, Cahill D G and Venkatasubramanian R 1997 Thermal conductivity of Si-Ge superlattices *Appl. Phys. Lett.* **70** 2957

[50] Giri A, Braun J L and Hopkins P E 2016 Effect of crystalline/amorphous interfaces on thermal transport across confined thin films and superlattices *J. Appl. Phys.* **119** 235305

[51] Wang X, Zhang J, Chen Y and Chan P K L 2017 Molecular dynamics study of thermal transport in a dinaphtho[2, 3-b:2′, 3′-f]thieno[3, 2-b]thiophene (DNTT) organic semiconductor *Nanoscale* **9** 2262–71

[52] Li B, Lan J and Wang L 2005 Interface thermal resistance between dissimilar anharmonic lattices *Phys. Rev. Lett.* **95** 104302

[53] Mu X, Zhang T, Go D B and Luo T 2015 Coherent and incoherent phonon thermal transport in isotopically modified graphene superlattices *Carbon* **83** 208–16

[54] Ravichandran J *et al* 2013 Crossover from incoherent to coherent phonon scattering in epitaxial oxide superlattices *Nat. Mater.* **13** 168